Method for Pole Figure Measurements Via a Dynamic Segmented Spiral Scheme

Surya Chandramouleeswaran[1, 2], Adam Creuziger[3], and Kip Findley[2]

[1]BASIS Chandler High School, 4825 South Arizona Ave. Chandler, Arizona 85248. USA
[2]Metallurgical and Materials Engineering Department, Colorado School of Mines, 1301 19th St, Hill Hall. Golden, CO 80401. USA.
[3]Materials Science and Engineering Division, Material Measurement Laboratory, National Institute of Standards and Technology, 100 Bureau Dr. Gaithersburg, MD 20899. USA.

October 6, 2022

Abstract

A new method for pole figure measurement is described, titled a Dynamic Segmented Spiral scheme. Compared to schemes currently in use, the dynamically segmented spiral scheme was shown to have advantages in term of evenness of pole figure coverage, and phase fraction accuracy. The phase fraction accuracy was shown to be robust for a variety of texture components commonly encountered in steels and for texture sharpness exceeding what is commonly encountered for rolled sheet steels. This scheme provides a promising alternative to conventional methods of simultaneous texture and phase fraction measurement.

Synopsis: A new method for pole figure measurement is described, titled a Dynamic Segmented Spiral scheme. This scheme provides a promising alternative to conventional methods of simultaneous texture and phase fraction measurement.

Keywords: Pole Figure, Phase Fraction, Neutron diffraction, Orientation distribution function, computational materials science

1 Background

Many engineering materials make use of multiple crystalline phases to produce properties that are an improvement upon what can be achieved by a single phase. Recent developments in materials science have enabled development of several classes of materials that take advantage of effects introduced by additional phases, one example of which are 3rd generation advanced high strength steels (3GAHSS) [1], [2], [3]. In addition to phase fraction information, crystallographic texture is another key parameter to quantify as the processing, production, use, and failure modes may depend on the arrangement of the microstructure. Therefore accurate measurement of both the phase fraction and texture are often key parameters for verification of material design and prediction of material behavior.

A common method for collecting and displaying crystallographic texture data are pole figures [4], [5]. Pole figures are a stereographic representation of intensity variations in a material, plotted for a particular *hkl* plane as a function of sample orientation. Sample orientation vectors for rolled sheets are often expressed in terms of the rolling direction (RD), transverse direction (TD), and normal direction (ND). Pole figures are typically collected by moving the sample through a series of rotations and *hkl* planes. A more complete representation of crystallographic texture, termed an an orientation distribution function (ODF), can be calculated using data from several pole figures through pole figure inversion techniques: spherical harmonics [4, 6], WIMV [7], EWIMV [8], and summation of radially symmetric functions [9]. These pole figure inversion techniques have been implemented in *PopLA* [10], *BEARTEX* [11], *MAUD* [12], and *mtex* [9].

Numerous laboratory diffraction instruments, synchrotron x-ray beamlines, and neutron beamlines can provide phase fraction and crystallographic texture measurements. Data from these instruments can often be used to simultaneously measure phase fractions and crystallographic texture. As many advanced materials use metastable phases, the traditional approach of powdering a sample will result in inaccurate phase measurements as some portion of the sample may transform into other phases. Phase fraction and stability are often functions of composition and processing, necessitating measurements on the material as produced. When diffraction data is recorded the phase fraction data is often calculated from a simple summation [13], [14] over all diffraction vectors (i.e., positions on a pole figure) measured. However, as shown in [14] and [15], summation alone can lead to bias in phase fraction. Bias errors were found to be negligible when the series of diffraction vectors were evenly distributed over a pole figure. Phase measurements that take the texture of the sample into account either by simultaneously fitting the texture and phase fraction (co-refinement) [16], [17], [18], [19] or by even measurement of the pole figure [15] should be more accurate.

Co-refinement algorithms applied to diffraction data typically rely on two alternating fitting sequences: first a fit of the texture and second a propagation of the texture values to each diffraction peak to modify the intensity as a function of the relative sample orientation. This technique has been routinely applied for several time of flight (TOF) neutron sources such as HIPPO [20], iMATERIA [21], TAKUMI [22], and NOMAD [23]. As shown for limestone sample investigated as part of a round robin [24], [25], it is possible to get consistent texture data from the co-refinement approach.

However, the phase fraction accuracy of the co-refinement technique has not been as extensively studied. As noted in several quantitative phase analysis round robins involving Rietveld refinement that do not add the additional complexity of texture effects (powdered materials), significant deviations can occur due to choices made by the operator [26], [27]. The large number of variables [27], dependence of accuracy on converged parameters across all data sets [28], complex procedure [20], and effect of order of refinement [29], have each been identified as contributing factors in these deviations. One advantage of complete and even pole figure measurement techniques to determine phase fraction is that the bias errors due to texture are accounted for without requiring Rietveld refinement. However, a disadvantage of the complete pole figure technique is that the number of peaks measured is typically fewer, which can introduce other errors in phase fraction measurements.

Electron backscatter diffraction (EBSD) is another technique that is routinely used for texture and phase fraction measurements [30]. This technique typically provides a spatial map of the phases and orientations present on a prepared surface. While growing in usage, there are a number of challenges for accurate measurements. For texture measurements, the number of grains required for accuracy estimated to be 10,000 [31]. Data sets and time required for each scan grow rapidly if the number of EBSD points per grain (> 100) suggested for grain size measurements [32] are recorded. Wright et al. [31] notes that differences in grain sizes between phases can cause additional challenges. The step size and data cleaning choices also likely have an impact on accuracy of the measurements, particularly if the phases have different grain sizes or shapes.

A series of diffraction vectors for texture measurements via pole figures has been termed a sampling scheme by Kocks et al. [5], which also includes some example sampling schemes. A well known sampling scheme is termed the equal angle grid, where the diffraction vectors are arranged in an even grid of angles (often a 5° resolution). As noted in Kocks et al., these equal angle grids result in an uneven distribution of pole figure area coverage [5]. The hexagonal grids of Matthies [33] and Rizzie [34] were developed to address the uneven area coverage. These grids have an additional benefit that for a given sampling scheme resolution they reduce the number of measurement points compared with an equal angle grid.

Prior to the use and development of equal angle and hexagonal sampling schemes, spiral sampling schemes were developed. As shown in some of the original work by Holden [35], and included in Klug & Alexander [36], these early spiral schemes were accomplished by mechanical linkages between the tilt and rotation motors. This arrangement results in a spiral that has a constant rate of expansion (i.e., an Archimedean spiral). While computer control of the x-ray goniometer stage has made mechanical linkages obsolete and therefore spiral techniques have fallen out of use, spiral schemes have the advantage of allowing continuous motion of the sample. However, the use a mechanical linkage for a spiral scheme (or reproduction via computer control) will likely result in uneven pole figure area coverage, similar to the equal angle grid shown in [5].

This paper demonstrates a new spiral scheme with even pole figure area coverage, termed a 'Dynamic Segmented Spiral'. The Dynamic Segmented Spiral scheme was developed to cover the pole figure space more evenly with the hypothesis that more even coverage will provide a more accurate phase fraction and texture measurement than other sampling schemes. The spiral motion also allows for simple summation and continuous motion, unlike more discrete schemes.

2 Methods

To eliminate additional sources of variation inherent in experimental data and analysis methods, this work uses simulated texture and phase data, as in [15]. In order to achieve complete pole figure coverage, the sampling schemes explored assume a transmission geometry. Figure 1 is an illustration of a goniometer and angle conventions used for neutron diffraction. The effects of incomplete pole figure coverage and intensity corrections from sample tilt, such as commonly encountered in a reflection geometry, is outside the scope of this work.

Four different sampling schemes were explored, the dynamic segmented spiral, the hexagonal grids of Matthies [33] and Rizzie [34], as well as the Holden [35] spiral scheme. The number and distribution of diffraction vectors are compared between the four sampling schemes, as well as ODF accuracy and accuracy of phase fraction by summation. For comparison, a common resolution parameter (ζ) was used in the construction of each sampling scheme. The code base developed in [15] was built upon in this work, with observations on even pole figure coverage from [14] used to inform the Dynamic Segmented Spiral scheme. The code used for this work is available at [37] as release version #2.2.0.

2.1 Definition of the Dynamic Segmented Spiral

To create a spiral with even pole figure area coverage, the pole figure sphere was divided into discrete spherical segments. As shown in [14], spherical segments provide a simple calculation for spherical area. The polar angle between each segment was defined by a resolution parameter (ζ). The spiral scheme iterates through a full goniometer rotation ($0° < \phi \leq 360°$) while the goniometer tilt (χ) range is limited within the range of each spherical segment. The initial point of the spiral was set at $\chi_0 = 90°$ and $\phi_0 = 0°$. The next step in the spiral is determined by the equations 1 to 5.

$$p = \frac{360°}{\zeta} \sin(\chi_{n-1}) \tag{1}$$

$$\phi_s = \frac{360°}{p} \tag{2}$$

$$\chi_s = \frac{\zeta}{p} \tag{3}$$

$$\phi_n = \phi_{n-1} + \phi_s \tag{4}$$

$$\chi_n = \chi_{n-1} - \chi_s \tag{5}$$

The step increments ϕ_s and χ_s are updated based upon the prior χ value. Any additional rotation beyond $\phi > 360°$ is also retained in this method whe moving to the next spherical segment. The tilt increment value is therefore small at the start of the spiral and increases continuously towards the center of the pole figure. This spiral scheme is termed a 'Dynamic Segmented Spiral' in the rest of this work.

2.1.1 Holden Spiral

The construction of the Holden spiral uses a constant rate of rotation for ϕ and a scaled rate of rotation for χ. The rate of expansion of the Holden spiral is set by the same resolution parameter (ζ) used in the Dynamic Segmented Spiral. Using the initial point $\phi_0 = 0\circ$ and for $\phi_n \leq 360° \frac{90°}{\zeta}$, the Holden spiral is defined by equations 6 and 7.

$$\phi_n = \phi_{n-1} + \zeta \tag{6}$$

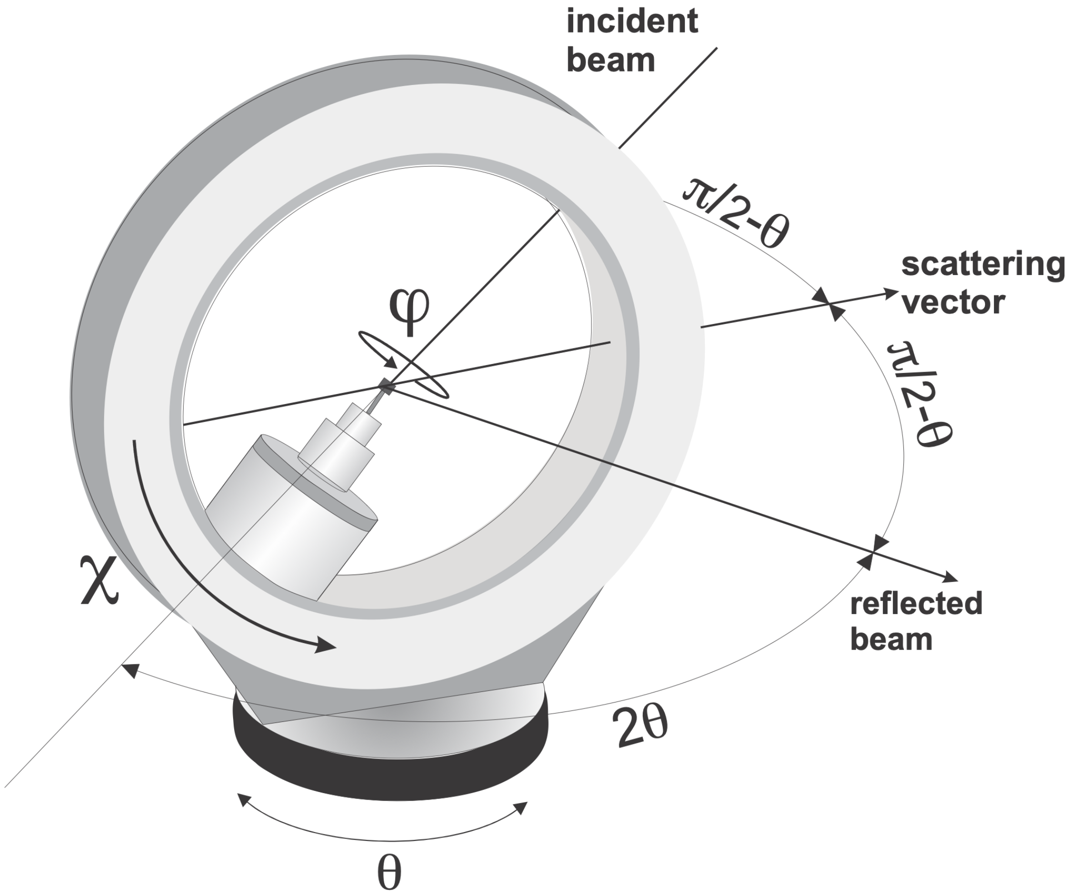

Figure 1: Sketch of a goniometer for pole figure measurements in a transmission geometry, with rotation (ϕ) and tilt (χ) axes labeled. Bragg angle (θ) is also shown, but not considered in this work. Courtesy of Thomas Gnaupel-Herold.

$$\chi_n = \phi_n \frac{\zeta}{360°} \tag{7}$$

2.1.2 Rizzie Hexagonal Grid

The construction of the Rizzie hexagonal grid described in equations 8 to 18 is largely identical to the description given in Rizzie [34] where a mesh of equilateral triangles is placed over an equal area pole figure. However, stereographic conversions for equal area [5] were explicitly added (replacing R in Rizzie [34] with D_{max}). χ_{max} was set equal to 90°. The resolution parameter (ζ) is used to determine the value of N:

$$N = \frac{90°}{\zeta} \tag{8}$$

The maximum value of tilt is converted to a D_{max} value using the equation for an equal area stereographic projection.

$$D_{max} = 2\sin(\frac{\chi_{max}}{2}) \tag{9}$$

To construct the grid, integer series j is used, with:

$$j = \{0, 1, 2, ...\} \tag{10}$$

and constructor function y_j defined as:

$$y_j = j * \frac{\sqrt{3}D_{max}}{2N} \tag{11}$$

The values for j are limited by the inequality:

$$|y_j| \leq D_{max} \tag{12}$$

A second integer series i takes values within the inequality:

$$i * \frac{D_{max}}{N} \leq \sqrt{(D_{max})^2 - (y_j)^2} \tag{13}$$

The constructor function x_{ij} takes the following values:

$$x_{ij} = \begin{cases} \frac{D_{max}}{N} i & \text{if j mod 2} = 0 \\ \frac{D_{max}}{2N} + \frac{D_{max}}{N} i & \text{if j mod 2} = 1 \end{cases} \tag{14}$$

The constructor functions are then used to calculate the tilt with an intermediate step:

$$D_{ij} = \sqrt{(x_{ij})^2 + (y_j)^2} \tag{15}$$

before using the inverse stereographic function to determine the tilt position (χ_{ij}):

$$\chi_{ij} = 2 \arcsin(\frac{D_{ij}}{2}) \tag{16}$$

The rotation position for the first and second quadrants of the pole figure are found from:

$$\phi_{ij} = \begin{cases} \arctan(\frac{y_j}{x_{ij}}) & \text{if } x_{ij} > 0 \\ 90° & \text{if } x_{ij} = 0 \\ \arctan(\frac{y_j}{x_{ij}}) + 180° & \text{if } x_{ij} < 0 \end{cases} \tag{17}$$

While the rotation positions for the third and fourth quadrants are found from:

$$\phi_{ij} = \begin{cases} \arctan(\frac{y_j}{x_{ij}}) + 180° & \text{if } x_{ij} > 0 \\ 270° & \text{if } x_{ij} = 0 \\ \arctan(\frac{y_j}{x_{ij}}) + 360° & \text{if } x_{ij} < 0 \end{cases} \tag{18}$$

2.1.3 Matthies Hexagonal Grid

The Matthies hexagonal grid is based on hexagonal tiles covering a pole figure, but is implemented as a series of concentric rings. The original reference for the Matthies hexagonal grid [33] does not include an explicit algorithm for how to construct the grid. However, this grid was implemented at the National Institute of Standards and Technology (NIST) Center for Neutron Research (NCNR) Residual Stress Diffractometer [38] and the algorithm provided to the authors. ζ is a resolution parameter as described above. In this case, the discretization occurs in the rotation n_ϕ and is described in equations 19 to 23.

$$n_\phi = \lfloor \frac{360°}{\zeta} \rceil \tag{19}$$

where $\lfloor \rceil$ indicates rounding to the nearest whole number. Similarly to the Rizzie Hex grid, two integer series are used in the grid construction, limited by the inequality $6 * i \leq n_\phi$ for i:

$$i = \{0, 1, 2, ..., \frac{n_\phi}{6}\} \tag{20}$$

and limited by the inequality $j \leq n_\phi - 6i$ for j:

$$j = \{1, 2, ..., (n_\phi - 6i)\} \tag{21}$$

The tilt and rotation positions are then set by:

$$\phi_{ij} = \frac{360^\circ}{n_\phi - 6i}(j-1) \tag{22}$$

$$\chi_{ij} = 2\arcsin(\frac{\sqrt{2}}{2}\frac{\frac{n_\phi}{6} - i}{\frac{n_\phi}{6}}) \tag{23}$$

While it is possible to move the sample continuously along a spiral path , for comparison with other sampling schemes, a discrete approach was used. The time required to traverse each spiral was divided into equal increments and the diffraction vector position at each increment was determined for both the Dynamic Segmented Spiral and the Holden spiral. Discretization also permits a calculation for the "number of points" as measured by the spiral schemes for comparison with the hexagonal grids. Experimentally, the total measurement time is expected to be a multiple of the number of points measured. In this work the additional time required for motor motion is not directly discussed, but the motor motion time is expected to correlate with the number of points measured. The code for each of these equations was implemented in [37] and available there for reference or use.

2.2 Sampling Scheme Comparison

To compare the evenness of pole figure area coverage, *oversampling plots* were created using the density contour function in the mplstereonet package [39]. This function discretizes the pole figure into small areas (each area is approximately 1 % of total hemisphere area) and computes the number of points inside each area (option 'Schmidt' in mplsteronet). The number of points per area are then normalized and depicted as a filled contour function. The values of the contour function represent the density of points, which is equivalent to the number of times a particular area is over sampled (values > 1), under sampled (values < 1) or evenly sampled ($= 1$).

To compare the distribution of diffraction vectors, histograms of the closest adjacent vector were calculated. A matrix of dot products for each vector series was computed, sorted by value, and the second term was retained (as the first term corresponds to 0, the vector dotted with itself). These histograms are expressed as a relative probability for comparison.

2.3 ODF Accuracy

Following the work described in [14] and [15], 20 common texture components for rolled steel sheets were used to assess accuracy of the ODFs. These texture components are separated into 7 face centered cubic (FCC) components for the austenite (γ) phase, and 13 body centered cubic (BCC) components for the ferrite (α) phase. These components are commonly encountered during rolling processes [40], [41] [5], [42] and were implemented via the texture analysis package *mtex* [9] with cubic crystal symmetry and orthotropic sample symmetry.

An ODF for each texture component was created, and pole figures using each of the four sampling schemes were calculated. Pole figures for the *hkl* planes (111), (200), and (220) for the austenite phase and the (110), (200), and (211) planes for the ferrite phase were chosen for this work. Using these pole figures and input, a recalculated ODF was created. The difference between the original ODF and the recalculated ODF was determined, and the mean difference was calculated for each texture component. For this analysis, the pole figure resolution parameter ζ was fixed at 5°, as was the halfwidth of the recalculated ODF at 5°to match the pole figure resolution.

The sharpness of individual texture components was also investigated. Texture sharpness was implemented by assigning variable halfwidth values to each of the individual texture components to create an orientation distribution function (ODF). A halfwidth range from 2.5° to 50° was analyzed in this work.

2.4 Phase Fraction Accuracy with Textured Data

As discussed previously in [14] and [15], crystallographic texture and oversampling can affect phase fraction measurements. The common ODF components listed in the previous section were also used to assess the accuracy of phase fractions determined by summation.

The phase fraction calculations follow the equations laid out in [14]. ODFs were used to calculate pole figures for a selection of *hkl* planes. Pole figure normalized intensity values $\hat{I}^{hkl}(\phi, \chi)$ for each *hkl* were extracted from these pole figures. Note that this intensity normalization is not the same as traditional normalization by the theoretical intensities, but solely based on texture and sampling effects. The pole figure normalized intensity bypasses sources of variation other than sampling scheme and crystallographic texture. Interpolated values were used when the needed (ϕ, χ) values were not coincident with the original pole figure grid. These pole figure normalized intensity values are in terms of multiples of a uniform (or random) distribution. For investigation of the bias errors in the phase fraction measurement, a known phase fraction was imposed on the data. In this work an austenite phase fraction (ξ) of 0.25 and ferrite phase fraction of 0.75 ($1 - \xi$) was used, matching values assumed in [15]. The austenite phase fraction V_γ is calculated from a rule of mixtures:

$$V_\gamma = \frac{\xi \hat{I}_\gamma}{\xi \hat{I}_\gamma + (1 - \xi)\hat{I}_\alpha} \tag{24}$$

where $\hat{I}_\gamma$ and $\hat{I}_\alpha$ are the average of all $\hat{I}^{hkl}(\phi, \chi)$ values measured for each phase.

As with the ODF reconstruction, the particular *hkl* planes used to calculate the phase fraction can impact the accuracy of phase fraction measurement [14], [15]. Common approaches include using intensity data from a select list of measured peaks or fitting the entire spectrum of data (i.e., Rietveld refinement). Evaluating the influence of which particular peak choice selections are optimal was outside the scope of this project. The *hkl* planes (111), (200), and (220) for the austenite phase and the (110), (200), and (211) planes for the ferrite phase were chosen as a benchmark for this work, as in the ODF reconstruction.

3 Results

3.1 Comparison of Sampling Schemes

A discrete representation of the Dynamic Segmented Spiral scheme is shown Figure 2a . Discrete representations of the spiral scheme of Holden (Figure 2b), the hexagonal grid of Rizzie (Figure 2c), and the hexagonal grid of Matthies (Figure 2d) are also shown. To facilitate comparison between schemes, each plot shown in Figure 2 uses a resolution of $\zeta = 5°$. Table 1 includes the number of discrete points generated for each of the four schemes with resolutions of $\zeta = 2.5°$, $\zeta = 5°$, and $\zeta = 10°$. Figure 3 shows oversampling plots for each scheme and a common resolution of $\zeta = 5°$. Histograms of the closest adjacent vector are shown in Figure 4.

As Figures 2a and 3a show, the Dynamic Segmented Spiral scheme has an even distribution of points across the pole figure. The points are arranged as nearly concentric rings with an offset set by ζ. The contour plot in Figure 3a indicates slight oversampling along the ND as well as along the periphery of the pole figure (RD-TD plane) on the top right and bottom left. The periphery in the top left and bottom right were slightly undersampled. The over and undersampling along the periphery is due to the proximity of the points to the $\chi = 90°$ boundary, which is a symmetry plane for the pole figure [39]. If the points are close to this boundary, they represent an oversampling, as shown by comparing 2a and 3a. Table 1 shows the Dynamic Segmented Spiral has fewer points than the Rizzie and Holden schemes but more than the Matthies scheme.

While the path of the Holden spiral is similar to the Dynamic Segmented Spiral, the rate at which the spiral completes one revolution is equal to the rate at which the spiral expands outwards. As shown in Figure 2b, the region along the ND is heavily clustered with sampling points, while the periphery of the scheme pole figure grid is more sparsely populated with sampling points. The oversampling plot in Figure 3b demonstrates this oversampling quite visibly along the ND, with a maximum value of 10, exceeding the upper bound of the color range common to the 3 plots. At $\zeta = 5°$ the Holden spiral samples 1297 points (Table 1), a greater number than any other sampling scheme explored in this work.

The Rizzie grid, shown in Figure 2c, samples the pole figure in a column-like arrangement of sampling points moving left to right on the pole figure as opposed to the nearly concentric rings of sampling seen on the spiral scheme grids in Figures 2a and 2b. Similar to the Dynamic Segmented Spiral shown in Figure 3a, the distribution of points for the Rizzie grid shown in Figure 3c is fairly even across the entire pole figure. There are small areas of undersampling at 60° incremental patches along the the $\chi = 90°$ boundary of the pole figure, corresponding to an 'edge' of the hexagonal grid. As listed in Table 1, the Rizzie grid has more points than the Dynamic Segmented Spiral, but fewer than the Holden spiral.

The Matthies hexagonal scheme shown in Figure 2d seems to blend concepts from both the spiral schemes and the Rizzie grid, adopting a concentric sampling pattern and a hexagonal arrangement of sampling points. However, the oversampling plot shown in Figure 3d indicates an oversampling by a factor of 2 along the outer ring of the pole figure. This oversampling is likely due to the points on the outer ring lying on the $\chi = 90°$ boundary, which is a symmetry line between upper and lower halves of the pole figures. The obvious advantage of this scheme is shown in Table 1 as the Matthies hexagonal scheme requires the fewest number of points of any scheme investigated, with approximately half the number of points as the Rizzie grid and Dynamic Segmented Spiral.

The histograms shown in Figure 4 provide additional details on the distribution of diffraction vectors. While each sampling scheme uses a common resolution parameter value of $\zeta = 5°$ in the construction of each scheme, the range and distribution of values are quite different between the schemes. For the Dynamic Segmented Spiral shown in Figure 4a, the median value of this distribution is 5.0° with a distribution narrowly grouped at 5°. A few adjacent vectors with a smaller angle can be seen with low relative probability. The Holden spiral shown in Figure 4b has a quite different distribution, with the relative probability initially sharply decreasing at smaller angles, but reaching a constant value between 3.0° and 0°. The median value of the Holden spiral is 3.5°. While the extent of the Rizzie hexagonal grid shown in Figure 4c is comparable to the Dynamic Segmented Spiral, the Rizzie hexagonalgrid has a wider spread near 5°, with a greater proportion of adjacent vectors smaller than 5°. The median value of the Rizzie hexagonal grid is 4.5°. The Matthies hexagonal scheme shown in Figure 4d has a similar spread as the Rizzie grid, but the Matthies hexagonal scheme is biased toward larger values of of adjacent vector angle. The median value for the Matthies hexagonal is 6.0°. There is also a significant distribution of values at 0° for the Matthies hexagonal scheme, supporting the oversampling plot 3d at $\chi = 90°$ values.

Scheme resolution	**Dynamic Segmented**	**Holden**	**Rizzie**	**Matthies**
2.5°	3303	5185	3805	1801
5.0°	828	1297	955	469
10.0°	209	325	241	127

Table 1: Summary of the number of sampling points for each tested scheme resolution.

3.2 Comparison of ODF Accuracy

The ODF reconstruction accuracy is shown in Table 2. Accuracy in ODF reconstruction was not greatly affected by sampling scheme. The Holden spiral performed slightly worse than the other three schemes for the entire range of component halfwidths. As expected, component halfwidths that were smaller than or equal to the sampling scheme resolution of $\zeta = 5°$ (and reconstructed ODF resolution of 5°) have significant errors. At component halfwidths greater than 30°, errors approach zero as there is minimal texture in the ODFs. As such halfwidth values greater than 30° are not included in Table 2.

Component Halfwidth	Dynamic Segmented	Holden	Rizzie	Matthies
2.5°	1.158	1.305	1.161	1.201
5.0°	0.235	0.321	0.235	0.238
10.0°	0.059	0.084	0.060	0.065
15.0°	0.045	0.069	0.046	0.049
20.0°	0.027	0.046	0.026	0.031
25.0°	0.025	0.032	0.025	0.027
30.0°	0.019	0.021	0.019	0.020

Table 2: ODF Error (mean difference) per sampling scheme and component halfwidth. ODF Error is caculated as an average for all components. Units of multiples of a uniform (random) distribution (MUD or MRD). Data uses a scheme resolution of $\zeta = 5°$ and reconstructed ODF halfwidth of 5°.

3.3 Comparison of Phase Fraction Accuracy

The oversampling plots suggest there may be bias errors in the phase fraction due to some regions of the pole figures being measured with greater frequency than others. Figure 5 shows the range of calculated phase fractions for each scheme. The range of phase fractions comes from calculations for all 91 (7*13) texture component combinations at each ODF halfwidth value. The scheme resolution ζ was held constant at 5° for each scheme. A 5 % relative error bound on the phase fraction was used as a benchmark for 'tolerable' error, as in [15]. While ODF halfwidth values up to 50° were investigated, the range of ODF halfwidths plotted in Figure 5 was reduced as the values converged at larger values of ODF halfwidth similar to Table 2. This method of plotting does not preserve which texture components are most significantly contributing to the variation. Heatmaps of the phase fraction for each texture combination are available in the supporting information that accompanies this paper.

The range of texture induced bias errors in the phase fraction calculation are comparable between the Dynamic Segmented Spiral and Rizzie grid schemes. For both, the range of bias errors are within the 5 % relative error bounds for ODF halfwidths greater than or equal to 5°. For the Matthies scheme, bias errors were nearly within a 5 % relative error bound for ODF halfwidths greater than or equal to 10°. The Holden spiral had errors that exceeded the 5 % relative error bound until an ODF halfwidth of 30°.

Restating these observations in a different way, for the Dynamic Segmented Spiral and Rizzie grid a scheme resolution of $\zeta = 5°$ was able to accurately measure phase fractions in materials with texture sharpness comparable to a halfwidth of 5°. For the Matthies grid, the scheme resolution of $\zeta = 5°$ was only able to accurately measure phase fractions in materials with texture sharpness comparable to a halfwidth of 10°. Finally, the Holden spiral was only able to accurately measure phase fractions in materials with texture sharpness comparable to a halfwidth of 30°. Inspection of the experimental ODFs in [5], [40], [41], [42] indicates texture sharpnesses on the order of ODF halfwidth 5° to 20° are commonly encountered.

4 Discussion

The Dynamic Segmented Spiral scheme was successfully demonstrated to have more even pole figure coverage than other schemes explored, comparable phase fraction accuracy to the Rizzie hexagonal scheme, and approximately 13 % fewer points than the Rizzie hexagonal scheme. This phase accuracy is largely due to the dynamic nature of updating the angular increment as a function of tilt and not forcing each segment to reset at 0° each rotation. In addition, unlike the Rizzie or Matthies schemes, the Dynamic Segmented Spiral can be run continuously, possibly allowing for additional data to be recorded while traversing the spiral. As Figure 4 shows, the Dynamic Segmented Spiral has tightest spread and median value that matches ζ.

There are significant disadvantages to the Holden spiral scheme compared to the Dynamic Segmented Spiral. While they both share a fundamental spiral pattern, the Dynamic Segmented Spiral offers significant improvements in measurement accuracy and measurement time. Given their common origin, they both experience some level of uneven sampling along the ND and along the periphery of the pole figure, but this unevenness is much greater in the Holden spiral. As the ND orientation corresponds directly with many common texture orientations, there were a several textures that impacted the ability for this scheme to effectively mitigate measurement error.

Comparing the Dynamic Segmented Spiral to the Rizzie grid, both schemes nearly evenly cover the pole figure. The Dynamic Segmented Spiral shows slight oversampling along the ND compared to the Rizzie grid, while the Rizzie grid has a few regions of undersampling arranged in a 60° pattern along the periphery of the pole figure. These differences account for the slight differences in which texture components cause bias errors. As noted, the Dynamic Segmented Spiral accomplishes even pole figure coverage with fewer measurement points. The motor motion for the Dynamic Segmented Spiral is also more continuous than the Rizzie grid, which requires more motor oscillation to reach each proscribed tilt angle.

The Matthies hexagonal scheme has a strong advantage over the Dynamic Segmented Spiral in the number of points required, as the Matthies hexagonal scheme samples nearly 50 % fewer points than both the spiral scheme and Rizzie hexagonal grid. However, the effective resolution of the Matthies hexagonal grid is 6° as shown in Figure 4d, despite using a resolution parameter of $\zeta = 5°$ In addition, the Matthies hexagonal scheme oversamples along the periphery of the pole figure, resulting in more bias errors that are more significant than the Dynamic Segmented Spiral or the Rizzie hexagonal scheme. This oversampling is due to the points lying on the $\chi = 90°$ symmetry boundary. While locating the points along the RD-TD plane is advantageous for pole figure measurements, weighting these points by a factor of 0.5 compared to interior points or only measuring $\phi \leq 180°$ (due to sample symmetry) may improve accuracy for phase fractions.

Despite all grids having a fixed scheme resolution ζ in this analysis, there are differences in the number of nearest neighbors and angular distance to neighboring points. The scatter plot for the Matthies grid (Figure 2d) visually appears less dense than the spiral (Figure 2a) and Rizzie hexagonal grid (Figure 2c). In general, the scheme resolution parameter generally does not match actual distribution. As Table 2 shows, the ODF accuracy does not strongly depend on scheme, up to resolution limit of the pole figure and/or ODF.

The Matthies hexagonal scheme correspondingly has larger phase fraction errors than the Rizzie hexagonal and Dynamic Segmented Spiral, and phase fraction errors outside the error bounds for halfwidths less than 10°. However, as many common rolling textures can be approximated by texture components with a halfwidth ranging from 10° to 20°, the advantage of fewer points may outweigh the decreased accuracy.

Reversing the criteria of scheme resolution and texture halfwidth, one can get an estimate of how sharp of a texture that a particular sampling scheme can resolve. In the cases of the Dynamic Segmented Spiral and Rizzie grids, the scheme resolution should be approximately half of the ODF halfwidth value. The texture literature currently offers little guidance on how best to assess if an ODF is artificially 'smoothed' due to the pole figure resolution.

5 Conclusions

This paper successfully demonstrated a new spiral scheme for conducting diffraction experiments. Compared to schemes currently in use, the dynamically segmented spiral scheme has advantages in term of evenness of pole figure coverage, number of points (time per measurement), and phase fraction accuracy. The phase fraction accuracy was shown to be robust for a variety of texture components commonly encountered in steels and for texture sharpness exceeding what is commonly encountered for rolled sheet steels. This scheme provides a promising alternative to conventional methods of simultaneous texture and phase fraction measurement, and takes advantage of modern computer control no longer requiring mechanical linkages.

6 Acknowledgements

The authors thank Michael Cox, Daniel Delgado Cornejo, and members of the NIST Center for Automotive Lightweighting for their advice and assistance. The authors also thank Thomas Gnaupel-Herold for providing the algorithm for the Matthies hexagonal and the goniometer sketch. This work was partially supported by the National Science Foundation Civil, Mechanical and Manufacturing Innovation Division (NSF-CMMI) award number 1728007. Adam Creuziger acknowledges the support of the National Institute of Standards and Technology (NIST), part of the United States Department of Commerce. Surya Chandramouleeswaran is especially grateful to: the Advanced Steel Processing and Products Research Center

(ASPPRC) at the Colorado School of Mines for extending him an internship opportunity and the chance to contribute towards this project, specifically ASPPRC Director Dr. John Speer, and ASPPRC students and staff for their guidance, support, and friendship; and the BASIS Chandler High School Senior Project Program, specifically his counselors and advisors, for supporting and advising him during the research period.

References

[1] Heung Nam Han, Chang-Seok Oh, Gyosung Kim, and Ohjoon Kwon. Design method for TRIP-aided multiphase steel based on a microstructure-based modelling for transformation-induced plasticity and mechanically induced martensitic transformation. *Materials Science and Engineering: A*, 499(1-2):462–468, January 2009.

[2] Emmanuel De Moor, PJ Gibbs, JG Speer, DK Matlock, and JG Schroth. Strategies for Third-Generation Advanced High-Strength Steel Development. *Iron & steel technology*, 7(3):132, 2010.

[3] Fadi Abu-Farha, Xiaohua Hu, Xin Sun, Yang Ren, Louis G. Hector, Grant Thomas, and Tyson W. Brown. In Situ Local Measurement of Austenite Mechanical Stability and Transformation Behavior in Third-Generation Advanced High-Strength Steels. *Metallurgical and Materials Transactions A*, 49(7):2583–2596, July 2018.

[4] Hans-Joachim Bunge. *Texture Analysis in Materials Science*. Bunge Estate, Wolfratshausen, digital edition edition, 2015.

[5] U. F. Kocks, C. N. Tomé, and Hans-Rudolf Wenk. *Texture and Anisotropy*. Cambridge Press, Cambridge UK, 1998.

[6] Ryong-Joon Roe. Description of Crystallite Orientation in Polycrystalline Materials. III. General Solution to Pole Figure Inversion. *Journal of Applied Physics*, 36(6):2024–2031, June 1965.

[7] Siegfried Matthies and G. W. Vinel. On the Reproduction of the Orientation Distribution Function of Textureized Samples from Reduced Pole Figures Using the Conception of a Conditional Ghost Correction. *Physica Status Solidi B*, 112:K111–K114, 1982.

[8] L. Lutterotti, D. Chateigner, S. Ferrari, and J. Ricote. Texture, residual stress and structural analysis of thin films using a combined X-ray analysis. *Thin Solid Films*, 450(1):34–41, February 2004.

[9] R. Hielscher and H. Schaeben. A novel pole figure inversion method: specification of the *MTEX* algorithm. *Journal of Applied Crystallography*, 41(6):1024–1037, December 2008.

[10] John S. Kallend, U. F. Kocks, A. D. Rollett, and H.-R. Wenk. popLA - An Integrated Software System for Texture Analysis. *Textures and Microstructures*, 14:1203–1208, 1991.

[11] H. R. Wenk, S. Matthies, J. Donovan, and D. Chateigner. BEARTEX: a Windows-based program system for quantitative texture analysis. *Journal of Applied Crystallography*, 31(2):262–269, April 1998.

[12] Luca Lutteroti. Maud: a Rietveld analysis program designed for the internet and experiment integration. *Acta Crystallographica A*, 56:s54, 2000.

[13] Chester F. Jatczak, John A. Larson, and Steve W. Shin. *Retained austenite and its measurements by X-ray diffraction: an information manual*. Society of Automotive Engineers, Warrendale, PA, 1980.

[14] Adam Creuziger, Thien Phan, and Darren Pagan. Refinements in phase fraction determination of textured alloys from transmission diffraction data. *Journal of Applied Crystallography*, 54(5):1480–1489, October 2021. G2021-0227.

[15] Adam Creuziger, Chris Calhoun, Whitney Poling, and Thomas Gnaupel-Herold. Assessment of Bias Errors Caused by Texture and Sampling Methods in Diffraction-Based Steel Phase Measurements. *Journal of Applied Crystallography*, 51:720–731, March 2018.

[16] H.-R. Wenk, L. Lutterotti, and S. Vogel. Texture analysis with the new HIPPO TOF diffractometer. *Nuclear Instruments and Methods in Physics Research Section A: Accelerators, Spectrometers, Detectors and Associated Equipment*, 515(3):575–588, December 2003.

[17] S. Matthies, J. Pehl, H.-R. Wenk, L. Lutterotti, and S. C. Vogel. Quantitative texture analysis with the HIPPO neutron TOF diffractometer. *Journal of Applied Crystallography*, 38(3):462–475, June 2005.

[18] Allen C Larson and Robert B Von Dreele. GSAS - General Structure Analysis System. Technical Report LAUR 86-748, Los Alamos National Laboratory, 2004.

[19] Brian H. Toby and Robert B. Von Dreele. *GSAS-II* : the genesis of a modern open-source all purpose crystallography software package. *Journal of Applied Crystallography*, 46(2):544–549, April 2013.

[20] H.-R. Wenk, L. Lutterotti, and S. C. Vogel. Rietveld texture analysis from TOF neutron diffraction data. *Powder Diffraction*, 25(3):283–296, September 2010.

[21] Yusuke Onuki, Takuro Masumura, Toshihiro Tsuchiyama, Shigeo Sato, Toshiro Tomida, and Setsuo Takaki. Mutual Verification of Phase Fraction Analysis Techniques for Steels Comprising Deformation Induced Martensite Phases: Neutron-Diffraction-Based Rietveld Texture Analysis and Saturation Magnetization Measurement. *Tetsu-to-Hagane*, 106(7):457–464, 2020.

[22] Pingguang Xu, Stefanus Harjo, Mayumi Ojima, Hiroshi Suzuki, Takayoshi Ito, Wu Gong, Sven C. Vogel, Junya Inoue, Yo Tomota, Kazuya Aizawa, and Koichi Akita. High stereographic resolution texture and residual stress evaluation using time-of-flight neutron diffraction. *Journal of Applied Crystallography*, 51(3):746–760, June 2018.

[23] N. E. Peterson, J. R. Einhorn, C. M. Fancher, J. R. Bunn, E. A. Payzant, and S. R. Agnew. Quantitative texture analysis using the NOMAD time-of-flight neutron diffractometer. *Journal of Applied Crystallography*, 54(3):867–877, June 2021.

[24] H. R. Wenk. Standard project for pole-figure determination by neutron diffraction. *Journal of Applied Crystallography*, 24(5):920–927, October 1991.

[25] L. Lutterotti, S. Matthies, H.-R. Wenk, A. S. Schultz, and J. W. Richardson. Combined texture and structure analysis of deformed limestone from time-of-flight neutron diffraction spectra. *Journal of Applied Physics*, 81(2):594–600, January 1997.

[26] Ian C. Madsen, Nicola V. Y. Scarlett, Lachlan M. D. Cranswick, and Thaung Lwin. Outcomes of the International Union of Crystallography Commission on Powder Diffraction Round Robin on Quantitative Phase Analysis: samples 1 *a* to 1 *h*. *Journal of Applied Crystallography*, 34(4):409–426, August 2001.

[27] T. G. Fawcett, F. Needham, J. Faber, and C. E. Crowder. International Centre for Diffraction Data round robin on quantitative Rietveld phase analysis of pharmaceuticals. *Powder Diffraction*, 25(1):60–67, March 2010.

[28] Sven C. Vogel, Chris M. Biwer, David H. Rogers, James P. Ahrens, Robert E. Hackenberg, Drew Onken, and Jianzhong Zhang. Interactive visualization of multi-data-set Rietveld analyses using *Cinema:Debye-Scherrer*. *Journal of Applied Crystallography*, 51(3):943–951, June 2018.

[29] Matthew R. Rowles. The effect of data quality and model parameters on the quantitative phase analysis of X-ray diffraction data by the Rietveld method. *Journal of Applied Crystallography*, 54(3):878–894, June 2021. arXiv:2008.11046 [cond-mat].

[30] Adam J. Schwartz, Mukul Kumar, Brent L. Adams, and David P. Field, editors. *Electron backscatter diffraction in materials science*. Springer, New York, 2nd ed edition, 2009. OCLC: ocn308158147.

[31] Stuart I. Wright, Matthew M. Nowell, and John F. Bingert. A Comparison of Textures Measured Using X-Ray and Electron Backscatter Diffraction. *Metallurgical and Materials Transactions A*, 38(8):1845–1855, July 2007.

[32] International Organization for Standardization, editor. *ISO 13067:2020(E) Microbeam analysis — Electron backscatter diffraction Measurement of average grain size*. ISO, Switzerland, July 2020.

[33] S. Matthies and Hans-Rudolf Wenk. Optimization of Texture Measurements by Pole Figure Coverage with Hexagonal Grids. *Physica Status Solidi A*, 133:253–257, 1992.

[34] Anthony C. Rizzie. Elaboration on the Hexagonal Grid and Spiral Method for Data Collection Via Pole Figures. Undergradute Research Report Vol 5, Ball State University, 2008.

[35] A. N. Holden. A Spiral-Scanning X-Ray Reflection Goniometer for the Rapid Determination of Preferred Orientations. *Review of Scientific Instruments*, 24(1):10–12, January 1953.

[36] Harold P. Klug and Leroy E. Alexander. *X-Ray Diffraction Procedures*. John Wiley & Sons Inc, 2nd edition, 1974.

[37] Adam Creuziger, Chris Calhoun, Whitney Poling, and Thomas Gnaupel-Herold. DataSet: Assessment of Bias Errors Caused by Texture and Sampling Methods in Diffraction-Based Steel Phase Measurements, April 2018. Commit 176069b.

[38] P.C. Brand, H.J. Prask, and T. Gnaeupel-Herold. Residual stress measurements at the NIST reactor. *Physica B: Condensed Matter*, 241-243:1244–1245, December 1997.

[39] Joe Kington. mplstereonet - Stereonets for matplotlib, 2015.

[40] I.L Dillamore and W.T Roberts. Rolling textures in f.c.c. and b.c.c. metals. *Acta Metallurgica*, 12(3):281–293, March 1964.

[41] Wolfgang Bleck, Rolf Großterlinden, Ulrich Lotter, and Carl-Peter Reip. Textures in steel sheets. *Steel Research*, 62(12):580–586, December 1991.

[42] Leo Kestens and John J. Jonas. Transformation and Recrystalization Textures Associated with Steel Processing. In *ASM Handbook*, volume 14A Metalworking: Bulk Forming, pages 685–700. ASM International, 2005.

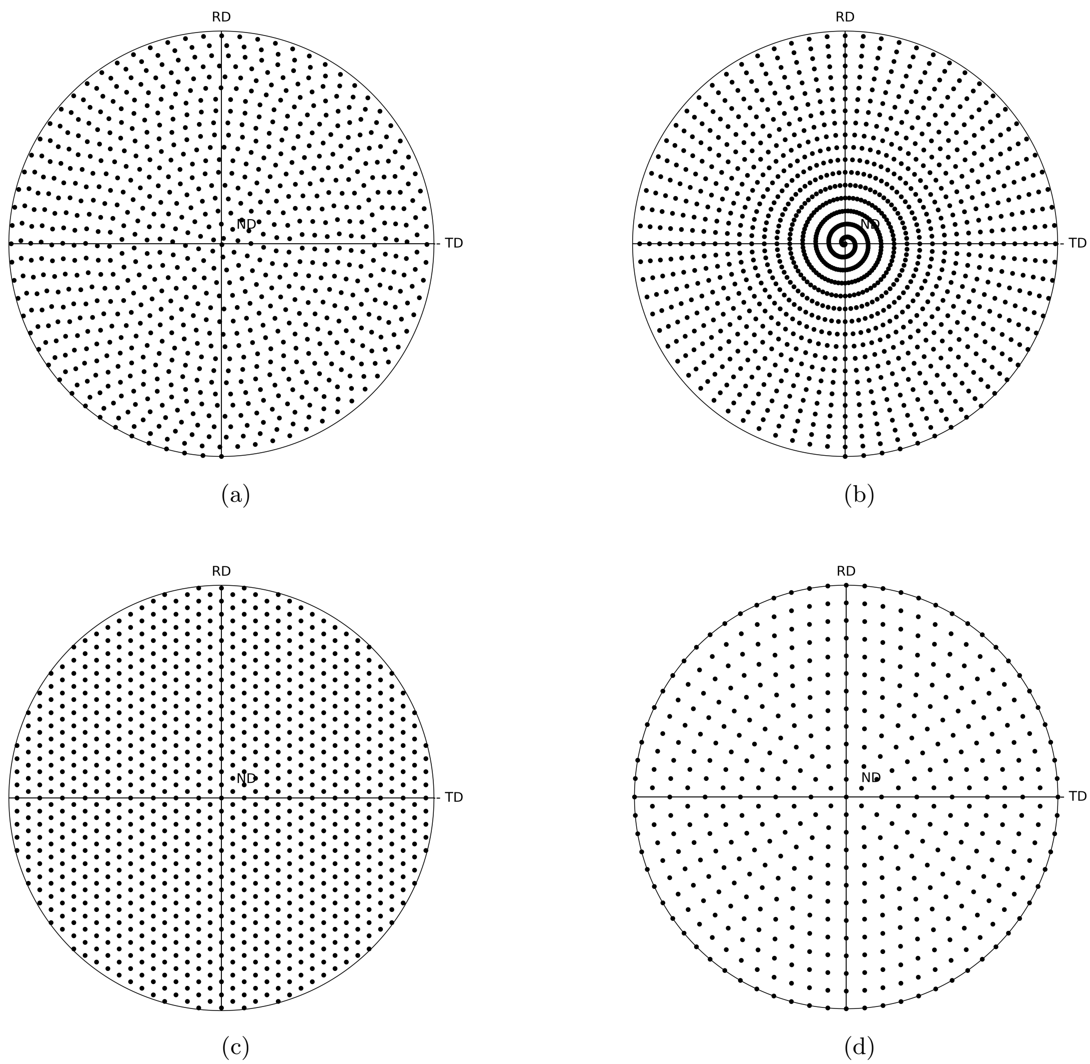

(a) (b) (c) (d)

Figure 2: Discrete scatter plot of the sampling schemes: (a) Dynamic Segmented Spiral (b) Holden Spiral (c) Rizzie grid (d) Matthies hexagonal scheme. Plotted on an equal area pole figure with axes x=rolling direction (RD), y=transverse direction (TD), and z=normal direction (ND). All plots use a scheme resolution of $\zeta = 5^{\circ}$ and an equal area stereographic projection

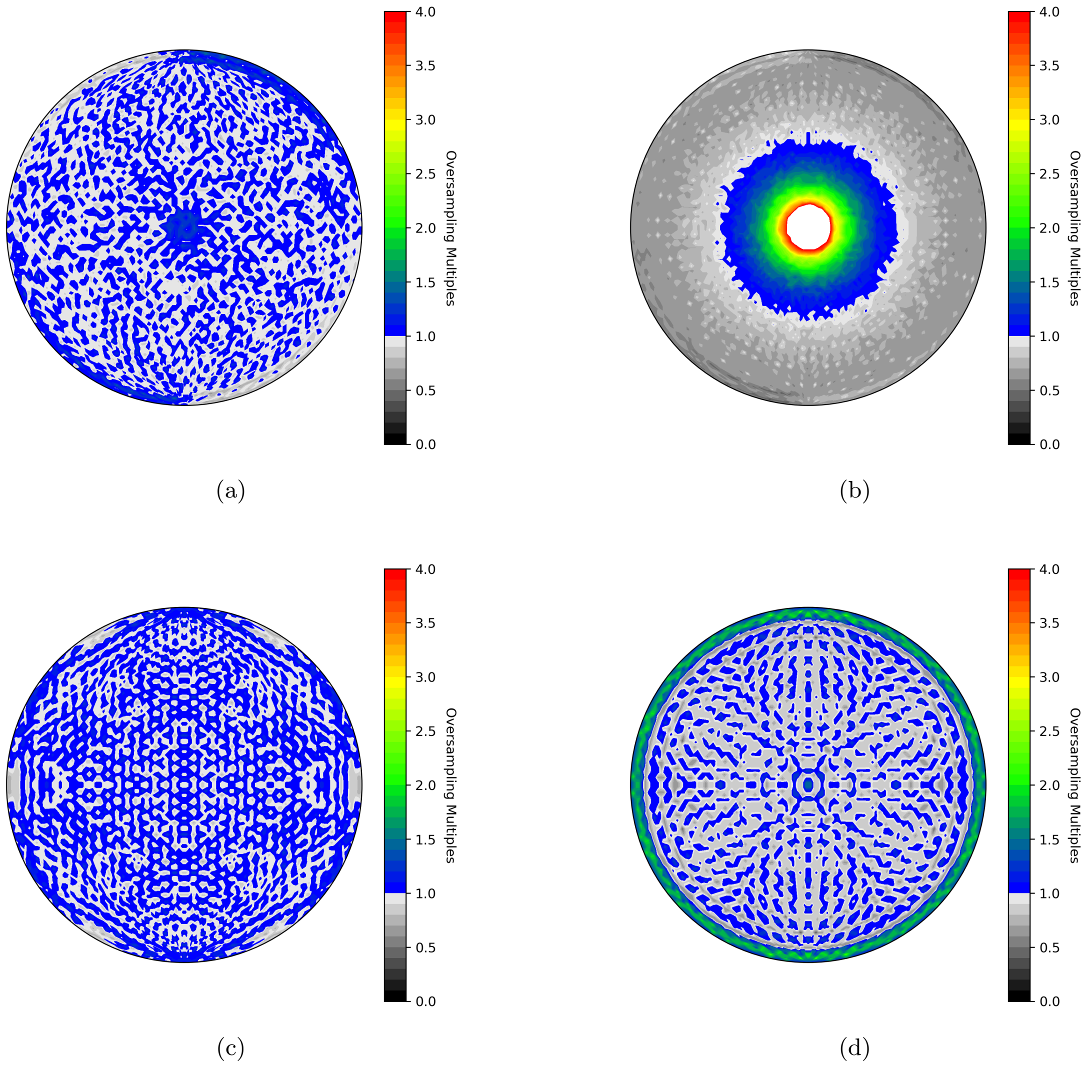

Figure 3: Filled contour plots of the sampling schemes: (a) Dynamic Segmented Spiral (b) Holden Spiral (c) Rizzie grid (d) Matthies hexagonal scheme. The color axis shows the oversampling multiple (density of points).

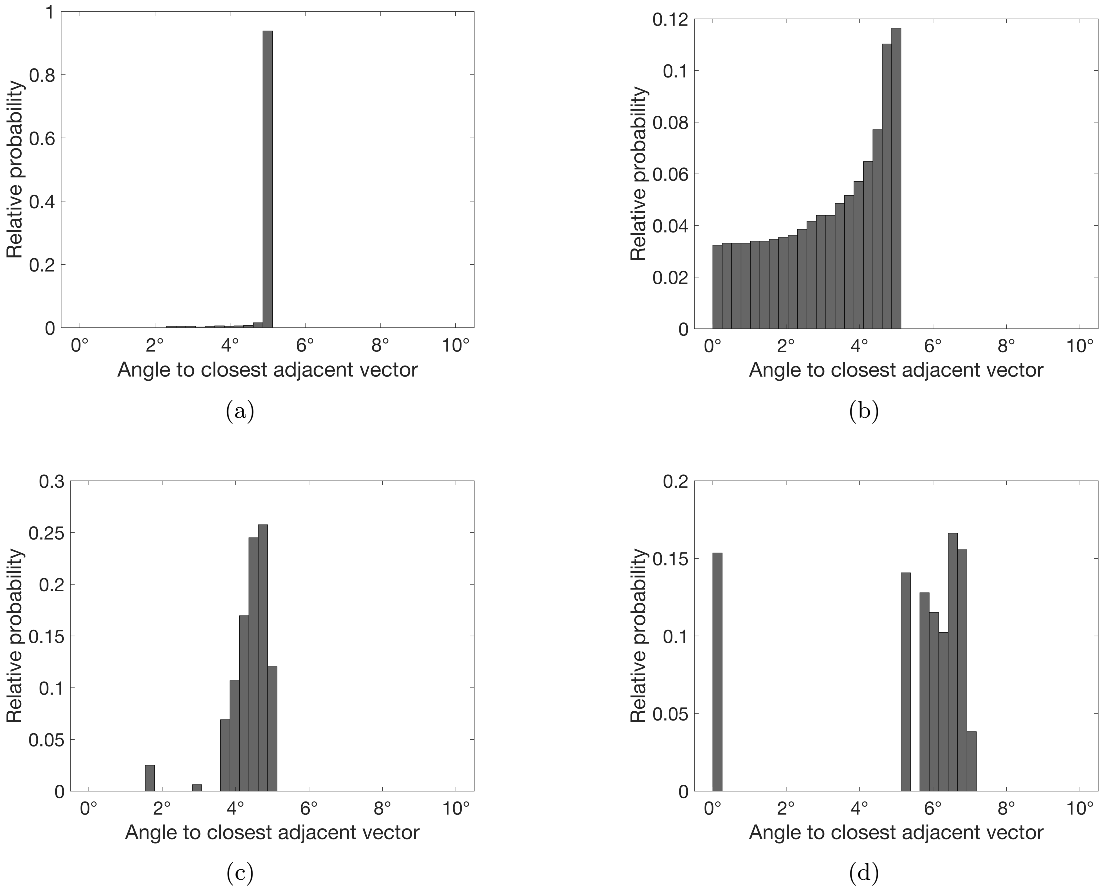

Figure 4: Normalized histograms showing the relative probability distribution of the angle to the closest adjacent scattering vector for sampling schemes: (a) Dynamic Segmented Spiral (b) Holden Spiral (c) Rizzie grid (d) Matthies hexagonal. All plots use a scheme resolution of $\zeta = 5°$. Note the Y axes scales are dissimilar to show details of the distribution.

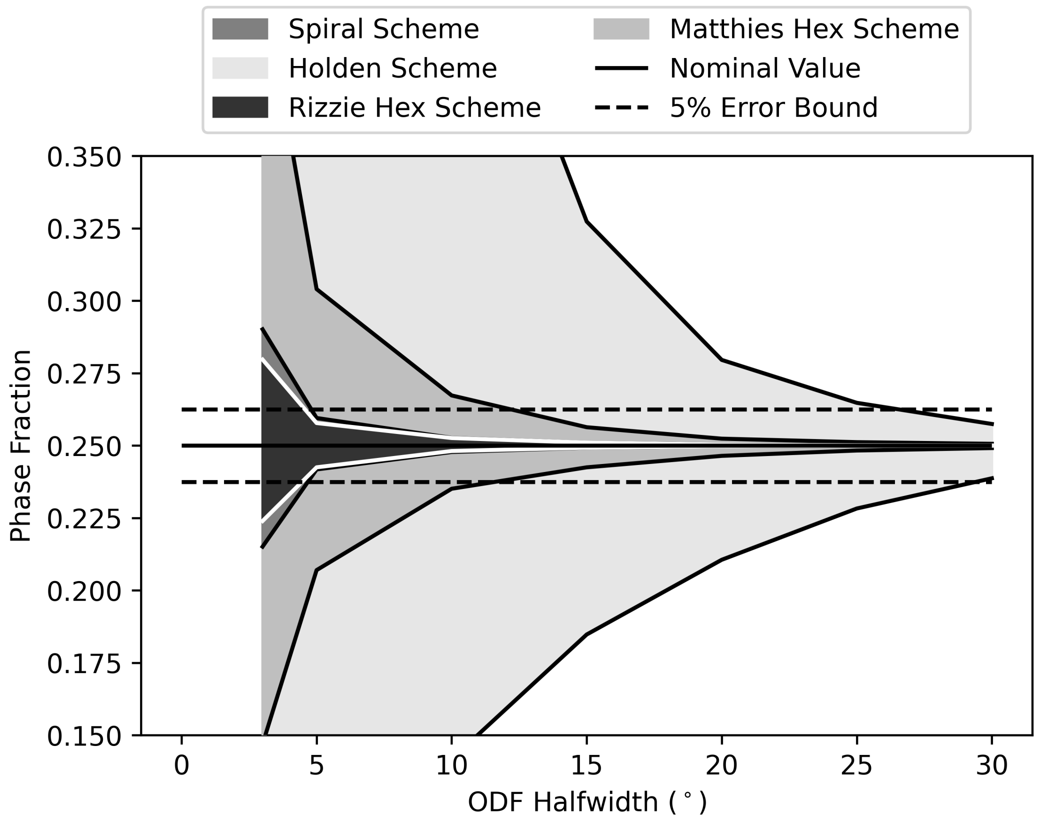

Figure 5: Comparison of phase fraction error range for all 4 schemes. The scheme resolution was fixed at $\zeta = 5°$.